**Research Article**
https://doi.org/10.1631/jzus.B2600515

# Cang-Fu-Dao-Tan Formula exerts positive multigenerational effects on the offspring of polyendocrine metabolic ovarian syndrome mouse model through alleviating uterine inflammation

Weihuan HU[1*], Fangfang WANG[1,2,3,4,5*], Meiping LI[1,6*], Ningning XIE[1], Shaoyan YE[7], Siwen ZHANG[7], Wenshan ZENG[1], Bizhen WANG[7], Lu ZHAO[8], Fan QU[1,2,3,4✉], Jue ZHOU[7✉]

[1]*Women's Hospital, School of Medicine, Zhejiang University, Hangzhou 310006, China*
[2]*Institute of Medical Genetics and Development, Key Laboratory of Reproductive Genetics (Ministry of Education) and Women's Hospital, Zhejiang University School of Medicine, Hangzhou 310006, China*
[3]*Zhejiang Provincial Key Laboratory of Traditional Chinese Medicine for Reproductive Health Research, Hangzhou 310006, China*
[4]*Zhejiang Key Laboratory of Maternal and Infant Health, Hangzhou 310006, China*
[5]*Linhai Branch, Women's Hospital, School of Medicine, Zhejiang University, Linhai 317000, China*
[6]*Shaoxing Maternity and Child Health Care Hospital, Maternity and Child Health Care Affiliated Hospital, Shaoxing University, Shaoxing 312000, China*[1]*Women's Hospital, School of Medicine, Zhejiang University, Hangzhou 310006, China*
[7]*School of Food Science and Biotechnology, Zhejiang Gongshang University, Hangzhou 310018, China*
[8]*Pharmaceutical Informatics Institute, School of Pharmacy, Zhejiang University, Hangzhou 310058, China*

**Abstract:** Background: Polyendocrine metabolic ovarian syndrome (PMOS), formerly known as polycystic ovary syndrome, is the most prevalent endocrine disorder among women of reproductive age. Cang-Fu-Dao-Tan formula (CFDTF), a traditional formula, has been reported to exert endocrine-metabolic regulatory effects in the treatment of PMOS. However, the effects and mechanisms by which CFDTF interrupts multigenerational PMOS-related features remain unknown. This study aimed to determine whether preconceptional CFDTF administration alleviates pathological phenotypes in the offspring of mothers with PMOS and to identify the potential underlying mechanisms. Methods: Prenatal anti-Müllerian hormone (PAMH)-induced PMOS mouse models (F0) were established, followed by preconceptional administration. Reproductive and glucolipid metabolic phenotypes were assessed in F1 and F2 offspring, and uterine transcriptomic profiling (RNA-seq) was performed in F0, F1, and F2 female offspring to investigate the potential mechanisms underlying CFDTF's effects. Results: Preconceptional CFDTF administration significantly ameliorated reproductive abnormalities across generations. In F0 – F2 females, it maintained estrous cyclicity, balanced testosterone levels, and reduced uterine inflammatory infiltration; in F1 males, it reduced abnormal seminiferous tubules. It also significantly improved glucolipid metabolism by lowering fasting glucose, total cholesterol, and hepatic lipid accumulation in F1 and F2 male and female offspring. RNA-seq analysis revealed multigenerational effects of preconceptional CFDTF administration on PMOS-associated uterine inflammatory signaling and immune microenvironment remodeling, which operate through a conserved cytokine network functionally linked to the interferon (IFN) inflammatory axis. Conclusions: Preconceptional CFDTF administration exerts positive multigenerational reproductive and glucolipid metabolic effects in a PMOS mouse model, through the alleviation of uterine inflammation.

**Key words:** Polyendocrine metabolic ovarian syndrome; Cang-Fu-Dao-Tan Formula; Multigenerational effects; Uterine inflammation.

## 1 Introduction

Polyendocrine metabolic ovarian syndrome (PMOS), formerly known as polycystic ovary syndrome

✉ Jue ZHOU, juezhou@zjgsu.edu.cn
Fan QU, syqufan@zju.edu.cn
The three authors contributed equally to this work
Jue ZHOU, https://orcid.org/0000-0002-0739-5151
Fan QU, https://orcid.org/0000-0003-1851-1514
Weihuan HU, https://orcid.org/0000-0002-3548-2797
Fangfang WANG, https://orcid.org/0000-0002-5957-1137
Meiping LI, https://orcid.org/0000-0002-5506-4007

Received July 13, 2026; Revision accepted Oct. 14, 2026;
Crosschecked xxx. xx, 20xx

© Zhejiang University Press 2026

Unedited

(Teede et al., 2026), affects approximately 11–13% of women worldwide, making it one of the most prevalent endocrine disorders among women of reproductive age (Stener-Victorin et al., 2024). The nomenclature was revised from PCOS to PMOS to emphasize that the syndrome is a systemic, polyendocrine and metabolic disorder involving multiple organs, rather than a condition confined to the ovaries (Teede et al., 2026). PMOS is characterized by insulin resistance and androgen excess and is closely associated with early-onset type 2 diabetes, cardiovascular risk, anovulatory infertility, and heightened risks of pregnancy complications (Stener-Victorin, et al., 2024). Despite its high prevalence, the underlying mechanisms remain incompletely understood, and treatment is still largely symptom-driven (Teede et al., 2023). Emerging evidence also suggests that PMOS may have multigenerational features, with maternal endocrine and metabolic disturbances potentially contributing to reproductive, cardiometabolic, and neurodevelopmental dysfunction in offspring (Risal et al., 2019; Risal et al., 2021).

One aspect of PMOS that has received growing attention is its effect on uterine function. Compared with healthy controls, women with PMOS exhibit endometrial differences, including chronic low-grade inflammation, impaired immune regulation, altered hormonal receptor expression, abnormal endometrial gene profiles, and disrupted vascular structure. All these factors can compromise embryo implantation and increase the risk of miscarriage (Palomba et al., 2021). A key mechanism driving this uterine dysfunction is androgen-driven immune dysregulation, with studies showing a drastic reduction of eosinophils in the uterus, along with higher frequencies of natural killer cells and elevated interferon (IFN)-γ and TNF-α levels in uterine tissue (Banerjee et al., 2023; Torstensson et al., 2024). These findings identify the uterus as a major site of androgen-mediated immune disruption in PMOS.

Cang-Fu-Dao-Tan formula (CFDTF) is a traditional Chinese medicine (TCM) dating back to the Ming dynasty. It contains a repertoire of bioactive compounds with independently documented anti-inflammatory, insulin-sensitizing, and androgen-modulating activities (Park et al., 2019; Wang et al., 2020; Yi et al., 2021; Liu et al., 2022; Yang and Zhou, 2025). Clinically, CFDTF-based therapy has been reported to improve pregnancy and ovulation rates in women with PMOS (Wu et al., 2022). Our group has also systematically characterized CFDTF's active constituents and elucidated their multi-target mechanisms in PMOS, providing a pharmacological foundation for its clinical application (Hu et al., 2024). Although CFDTF has been shown to alleviate PMOS symptoms, the effects and mechanisms by which CFDTF interrupts the transmission of PMOS-related features across generations are unknown. This study investigates whether preconceptional CFDTF administration can alleviate pathological phenotypes in the offspring of mothers with PMOS and explores the potential underlying mechanisms.

Under Peer Review

## 2 Materials and methods

### 2.1 Animals and ethical approval

All experimental procedures were approved by the Animal Ethics Committee of MSLT BIOTECH (Hangzhou) Co., Ltd. (Approval No. 2023H311106) and conducted in accordance with the Animal Research: Reporting of In Vivo Experiments (ARRIVE) 2.0 guidelines (Percie Du Sert et al., 2020). Female *C57BL/6J* mice (13 weeks old, body weight 18–22 g) were obtained from Beijing Vital River Laboratory Animal Technology Co., Ltd. (Beijing, China). Mice were housed in groups of 5–6 per individually ventilated cage, with bedding, nesting material, and shelter provided as environmental enrichment. Animals were maintained under a 12 h light/dark cycle (lights on at 08:00 h) at 22 ± 2° C with ad libitum access to standard chow and water. All mice were acclimated for one week prior to experimental manipulation.

### 2.2 Preparation and administration of CFDTF

The CFDTF comprised nine TCM herbs: *Atractylodes lancea (Thunb.) DC.* (Cangzhu, 10 g), *Cyperus*

*rotundus L.* (Xiangfu, 10 g), *Citrus reticulata Blanco* (Chenpi, 15 g), *Poria cocos (Schw.) Wolf* (Fuling, 15 g), *Arisaema erubescens (Wall.) Schott* (Tiannanxing, 10 g), Citrus aurantium L. (Zhike, 10 g), *Pinellia ternata (Thunb.) Makino* (Banxia, 10 g), *Zingiber officinale Roscoe* (Shengjiang, 10 g), and *Glycyrrhiza uralensis Fisch.* (Gancao, 10 g). All herbs were purchased as processed decoction pieces from Hangzhou Huadong Chinese Medicine Pieces Co., Ltd. (Hangzhou, China).

We authenticated the botanical identity and quality of each herb in accordance with the Chinese Pharmacopeia (2020 edition) and the *Zhejiang Provincial Processing Standards for Chinese Materia Medica* (2015 edition), using macroscopic, microscopic, and chromatographic (thin-layer chromatography [TLC]/high-performance liquid chromatography [HPLC]) methods. Table S1 provides detailed information regarding botanical origin, source region, authentication methods, batch numbers, and chemical marker contents. Each 100 g batch of herbs was decocted twice in distilled water at 100° C, first at a 1:10 (w/v) ratio for 1 h and then at a 1:8 (w/v) ratio for 45 min. The combined extracts were filtered, concentrated under reduced pressure, and lyophilized (Scientz, Ningbo, China). The extraction yield was approximately 10% (w/w), corresponding to a drug–extract ratio (DER) of 10:1. The lyophilized powder was stored at -20° C and reconstituted in normal saline before use. For quality control, the freeze-dried CFDTF powder was dissolved in methanol, filtered through a 0.22 μm membrane, and analyzed at Zhejiang University using HPLC. Representative chromatographic fingerprints are depicted in Fig. S1. Hesperidin and naringin were selected as marker compounds and identified using authenticated reference standards (Table S2).

The daily dose for each mouse was calculated using the body surface area (BSA) normalization method (Nair and Jacob, 2016). The standard human dose is 100 g of crude herb per day for a 60 kg adult. Applying a conversion coefficient of 12.3, the equivalent mouse dose was 20.5 g/kg/d (crude herb equivalent), corresponding to 2.05 g/kg/d of the lyophilized powder. The exact dosage should be further calculated based on the amount of lyophilized powder obtained from each batch of the herbal preparation.

### 2.3 Establishment of the PAMH model and experimental grouping

We used the prenatal anti-Müllerian hormone (PAMH) model to recapitulate human PMOS, following the protocol as previously described (Tata et al., 2018; Mimouni et al., 2021). Timed-pregnant *C57BL/6J* dams at embryonic day E14.5–E15.5 were randomly assigned to two prenatal treatment arms: (i) Control (phosphate-buffered saline [PBS], intraperitoneal injection [i.p.], n = 6 dams) and (ii) PAMH (recombinant human AMH at 0.12 mg/kg/day, i.p., n = 12 dams), administered daily from E16.5 to E18.5. This injection window was selected to coincide with the period of maximal testosterone sensitivity in the developing female hypothalamic–pituitary–gonadal (HPG) axis (Tata, et al., 2018).

Female founder-generation (F0) offspring were weaned at postnatal day (P) 21 and were subsequently randomized into three experimental groups at P60: (i) F0-Control (PBS; PBS-injected dam offspring receiving vehicle gavage, n = 6); (ii) F0-PMOS (PAMH; PAMH dam offspring receiving vehicle gavage, n = 6); and (iii) F0-CFDTF (PAMH + CFDTF; PAMH dam offspring receiving CFDTF by oral gavage, n = 6). Vehicle or CFDTF was administered once daily for 4 weeks; then F0 females were mated with untreated wild-type *C57BL/6J* males. Female first-generation (F1) offspring were raised to P90 without further treatment and were subsequently mated with naïve males to generate second-generation (F2) offspring. F2 female offspring were also raised to adulthood. After each generation, all breeders were replaced to avoid confounding by paternal PMOS exposure. We did not perform any formal a priori power calculation to determine sample size (Percie Du Sert, et al., 2020), instead the sample size was chosen based on previous studies using comparable PAMH models, our preliminary observations, and the group sizes commonly used in similar in vivo studies (Tata, et al., 2018; Mimouni and Giacobini, 2021; Mimouni, et al., 2021). Offspring were selected from multiple litters, and the number of offspring contributed by each litter was balanced across experimental groups to minimize potential litter effects.

At approximately 25 weeks of age, F0–F2 mice from all groups were euthanized using consistent protocols. Mice were anesthetized using isoflurane (RWD Life Science, China), and terminal blood was collected via retro-orbital puncture. After clotting, serum was harvested by centrifugation and stored at -80° C for further analysis, including testosterone level measurement. Following blood collection, animals were euthanized via $CO_2$ inhalation. Representative organs were harvested, and specific portions were fixed in 4% paraform-

Unedited

aldehyde for histological evaluation; the remaining tissues were snap-frozen in liquid nitrogen and stored at -80° C for molecular processing. All female mice were euthanized at the diestrus stage and males at the equivalent circadian time point to minimize estrous cycle-dependent variation in serum hormone levels and histological parameters.

### 2.4 In vivo systematic evaluation of reproductive and metabolic phenotypes in offspring

We monitored estrous cyclicity exclusively in female offspring for 14 consecutive days beginning at P70 using daily vaginal lavage cytology. Smears were stained with 0.1% crystal violet and classified as proestrus, estrus, metestrus, or diestrus based on the predominant cell type (Byers et al., 2012).

At approximately 25 weeks of age, F0–F2 mice from all groups were euthanized, and terminal blood was collected to obtain serum. Before sacrifice, and after a 12 h fast, we measured fasting blood glucose and performed an oral glucose tolerance test (OGTT) using a glucometer (Accu-Chek, Roche). Serum testosterone levels were measured at diestrus in females and at the equivalent circadian time point in males using species-specific enzyme-linked immunosorbent assay (ELISA) kits (EM1850, FineTest, China). We quantified serum profiles of total cholesterol (TC), triglycerides (TG), high-density lipoprotein cholesterol (HDL-C), and low-density lipoprotein cholesterol (LDL-C), total bile acids (TBA), total bilirubin (TBIL), and direct bilirubin (DBIL) using colorimetric or enzymatic assay kits (Nanjing Jiancheng Bioengineering Institute, China), following the manufacturer's instructions. For histomorphological assessment, ovarian, uterine, testicular, and subcutaneous adipose tissues were fixed in 4% paraformaldehyde, paraffin-embedded, sectioned at 5 μm, and stained with hematoxylin and eosin (H&E). We classified seminiferous tubules as abnormal when they exhibited a small or irregular lumen with loss of the normal stratified germinal epithelium, containing only a single layer of Sertoli cells or a few scattered germ cells, a focal Sertoli-cell-only-like pattern that resembles the histology described in mouse models of impaired spermatogenesis (Nakamoto et al., 2004). Ovaries were serially sectioned at 5 μm thickness; one section was sampled every nine consecutive sections to avoid repeated counting of the same follicle. We counted ovarian cystic follicles, corpora lutea, and antral follicles separately under light microscopy and estimated the total per ovary by multiplying the number counted by 10 (Swindells et al., 2026). Cystic follicles were defined as large fluid-filled structures exceeding the diameter of healthy late antral follicles, with a thinned granulosa cell layer, no identifiable oocyte, and occasional theca layer condensation (Myers et al., 2004). Because whole-ovary follicle counting requires exhaustive serial sectioning, fewer ovaries were processed for this analysis than for histological endpoints assessed on single sections. Liver tissues were cryosectioned at 8–10 μm and stained with Oil Red O to assess neutral lipid deposition. A detailed description of the methods used for quantifying average adipocyte size and the relative area of lipid droplets is provided in the Supplementary Material (Methods). All histological analyses were performed by an observer blinded to group assignment, and the prepared slides were scanned for subsequent analysis. For each mouse, one tissue section was analyzed, and the counts from all microscopic fields of that section were averaged to generate a single value per animal; these animal-level values were used for statistical analysis to avoid pseudo replication.

### 2.5 Uterine transcriptomic profiling (RNA-seq)

Uterine horns were collected at diestrus phase, snap-frozen, and stored at -80°C. Total RNA was extracted from homogenized uterine tissue using the TRIzol reagent (Invitrogen, USA), with quality verified using an Agilent 2100 Bioanalyzer (A260/280 ≥ 1.8 and RIN ≥ 7.0). Four biological replicates were sequenced for each group and generation, and all samples were processed and sequenced in a single batch. RNA-seq library construction and 150-bp paired-end sequencing were performed by LC-Bio Technologies (Hangzhou, China) on an Illumina NovaSeq 6000 platform. Bioinformatic analysis was conducted using the OmicStudio platform (Lyu et al., 2023).

To systematically characterize uterine transcriptional remodeling and its transgenerational propagation, we implemented an integrative bulk RNA-seq analytical framework combining differential expression analysis, single-sample pathway activity inference, and cross-generation concordance assessment. Differentially expressed genes (DEGs) were identified using a threshold of $|\log2FC| \geq 1.0000$ and $q < 0.05$ (where q rep-

Uncorrected

resents the adjusted *P*-value). Functional enrichment and molecular signature identification were performed via Gene Ontology (GO), Kyoto Encyclopedia of Genes and Genomes (KEGG) pathway analyses, and Gene Set Enrichment Analysis (GSEA) ($q < 0.05$). To quantify higher-order biological states, we conducted Gene Set Variation Analysis (GSVA) on MSigDB hallmark gene sets, focusing specifically on inflammatory and immune signaling. An IFN module score was calculated as the mean of Z-score-normalized GSVA enrichment scores for IFN-α response and IFN-γ response hallmarks per sample.

$$IFN\ module\ score = [Z\ (GSVA\text{- }IFN\text{-}\alpha) + Z\ (GSVA\text{- }I\ IFN\text{-}\gamma)] / 2.$$

### 2.6 Rescue gene identification and rescue signature scoring

Unlike GSVA or GSEA, which assess the activity of predefined gene sets, the rescue score is data-driven. It is calculated using only genes empirically identified as dysregulated in the disease model and reversed by the treatment, thereby directly quantifying treatment-induced transcriptional normalization at the individual-sample level. The combined z-score formulation follows the established single-sample gene-set scoring framework (Hanzelmann et al., 2013; Foroutan et al., 2018). First, we identified DEGs between Control and PMOS to capture model-associated transcriptional perturbations, and between CFDTF and PMOS to capture treatment-associated changes. Genes that were significantly dysregulated in both comparisons and changed in opposite directions were defined as rescue genes and classified by direction:

- **Rescue-up genes**: downregulated in Control vs. PMOS ($log2\ FC_{PMOS/Control} < -1$, *adjusted* $P < 0.05$) and upregulated in CFDTF vs. PMOS ($log2\ FC_{CFDTF/PMOS} > 1$, *adjusted* $P < 0.05$).
- **Rescue-down genes:** upregulated in Control vs. PMOS ($log2\ FC_{PMOS/Control} > 1$, *adjusted* $P < 0.05$) and downregulated in CFDTF vs. PMOS ($log2\ FC_{CFDTF/PMOS} < -1$, *adjusted* $P < 0.05$).

Only a directional reversal was required, and CFDTF expression levels were not required to approach those of the Control group. This inclusive, direction-based definition was used to capture coordinated but potentially subtle transcriptional shifts that converge on pathway-level restoration.

A rescue score was calculated for each sample to quantify transcriptional restoration. Across all samples, gene expression values were standardized for each gene to obtain z-scores:

$$Z_{ig} = (xig - \mu g) / \sigma g,$$

where xig is the expression of gene g in sample i, and $\mu$ g and $\sigma$ g are the mean and standard deviation across all samples. The rescue score for each sample was then computed as:

$$Rescue\ score_i = mean\ (Z_{i,Rescue\text{-}up}) - mean\ (Z_{i,Rescue\text{-}down}),$$

where $mean\ (Z_{i,Rescue\text{-}up})$ and $mean\ (Z_{i,Rescue\text{-}down})$ represent the mean z-scores over the rescue-up and rescue-down gene sets, respectively. A higher Rescue score indicates stronger transcriptional restoration toward the control state (Foroutan, et al., 2018). This strategy is conceptually consistent with the combined z-score framework used in single-sample gene-set scoring (Hanzelmann, et al., 2013).

### 2.7 Hub rescue gene identification

Rescued genes from each generation were mapped to the STRING database (confidence score > 0.4) to construct protein–protein interaction (PPI) networks (Szklarczyk et al., 2023). Key nodes within each network were then identified using the cytoHubba plugin in Cytoscape (v3.10.4) (Chin et al., 2014). To ensure robustness, we calculated top-ranked nodes using the Maximal Clique Centrality (MCC), Maximum Neighborhood Component (MNC), and Degree algorithms. The intersection of these three ranking methods was defined as the final rescue hub gene set for downstream analysis.

### 2.8 Candidate gene identification

Genes shared among the three consistently enriched KEGG pathways (mmu05323—Rheumatoid Arthritis; mmu05321—Inflammatory Bowel Disease; and mmu04060—Cytokine-cytokine receptor interaction) were intersected with hub genes from each generation. Candidate genes were further filtered by significant correlation with the IFN module score (Pearson r, $p < 0.05$).

Under Review

### 2.9 Immune cell infiltration analysis

To characterize the uterine immune microenvironment across generations, we conducted immune cell infiltration analysis separately for each generation using ImmuCellAI-mouse in the OmicStudio platform (Newman et al., 2015; Miao et al., 2022; Lyu, et al., 2023). We compared immune cell fractions within each generation using one-way analysis of variance (ANOVA), followed by Tukey's honest significant difference (HSD) post hoc test.

### 2.10 Immunohistochemical staining and quantitative real-time PCR (RT-qPCR)

Paraffin-embedded uterine tissues from F0, F1, and F2 female offspring were sectioned, deparaffinized, and rehydrated, then subjected to antigen retrieval. After blocking endogenous peroxidase activity and nonspecific binding, the sections were incubated with primary antibodies of *Tnf* (17590-1-AP, Proteintech, China), *Il17a* (ER1902-37, HUABIO, China), *Il1a* (ER1802-36, HUABIO, China), *Tgfb1* (81746-2-RR, Proteintech, China), and *Cd68* (83014-5-RR, Proteintech, China) overnight at 4° C and then with HRP-conjugated secondary antibodies. Immunoreactivity was visualized using DAB, and nuclei were counterstained with hematoxylin. Images were captured under a light microscope (dScan-D240 slide scanner (Dingjia, China), and staining intensity was quantified using ImageJ (version 1.54p). For each sample, at least three microscopic fields were randomly selected from one section per animal and analyzed. We averaged measurements across fields to obtain a single value per animal, and used these animal-level means for statistical analysis.

Total RNA was extracted from uterine tissues (n = 6 per group) using TRIzol reagent (Takara, Japan) according to the manufacturer's instructions. RNA concentration and purity were assessed using a NanoDrop spectrophotometer (Thermo Scientific, USA), and samples with an A260/A280 ratio of between 1.8 and 2.1 were used for subsequent analysis. The syntheses of the first-strand cDNA and real-time PCR quantitation were performed according to the manufacturer's instructions (RR047A and RR420A, Takara, Japan) on a Roche LightCycler 480 II system. Relative mRNA expression was calculated using the $2^{-\Delta\Delta Ct}$ method and normalized to *Gapdh* as the internal reference. Primer sequences are listed in the Supplementary Materials.

### 2.11 Statistical analysis

Phenotypic data are expressed as mean ± standard deviation (SD). Multiple group comparisons were performed using one-way ANOVA followed by Tukey's HSD post hoc test. All repeated-measures data (e.g., OGTT, weight change) were analyzed using two-way repeated-measures ANOVA with the Greenhouse–Geisser correction to account for potential violations of the sphericity assumption, followed by Tukey's multiple comparisons test. The Greenhouse–Geisser epsilon (ε) is reported where the correction was applied. All statistical analyses for phenotypic data were performed in GraphPad Prism v9.5 (GraphPad Software, San Diego, CA, USA). We considered $P < 0.05$ (two-tailed) statistically significant.

## 3 Results

### 3.1 Effects of CFDTF on the PMOS reproductive phenotypes of the PAMH-induced model mice

To evaluate CFDTF's multigenerational effects, we established the PMOS model in the F0 generation and generated female and male F1 (F1F and F1M, respectively) and F2 (F2F and F2M, respectively) offspring, as shown in Fig. 1a. Histological analysis confirmed that preconceptional CFDTF administration attenuated the anovulatory phenotype in the F0-PMOS group, decreasing the number of total antral follicles and cystic follicles (Figs. 1b and 1c). Preconceptional CFDTF administration also significantly rescued the disrupted estrous cyclicity in F0-PMOS mice (Fig. 1d). This cyclic abnormality was characterized by shortened metestrus and diestrus phases, coupled with a prolonged estrus phase (Fig. 1e). Consistent with the restoration of ovarian function, endocrine profiling revealed that CFDTF treatment significantly lowered the elevated serum testosterone levels in F0-PMOS mice (Fig. 1h). With respect to metabolic profile, preconceptional CFDTF

Unedited

intervention markedly attenuated the endpoint body weight gain in F0-PMOS mice (Fig. 1i), reduced hepatic lipid deposition (Figs. 1f and 1g), and normalized the aberrant serum profiles of TC, TG, LDL and HDL (Fig. 1j; all $P<0.05$). CFDTF administration also significantly improved fasting blood glucose and glucose tolerance in the OGTT (Figs. 1m-1o; $\varepsilon = 0.5855$ for the F0 OGTT analysis). Histopathological examination of uterine tissues revealed increased cellularity within the uterine stromal/myometrial compartments (Fig. 1k). Immunohistochemical staining further showed abundant *CD68*-positive macrophage-associated signals in the uterine tissues of F0-PMOS mice, which were significantly reduced by preconceptional CFDTF administration (Figs. 1k and 1l). Collectively, these findings indicate that preconceptional CFDTF administration effectively rescues the primary PMOS phenotype in the F0 generation, providing a foundation for further assessment of its protective effects across subsequent generations.

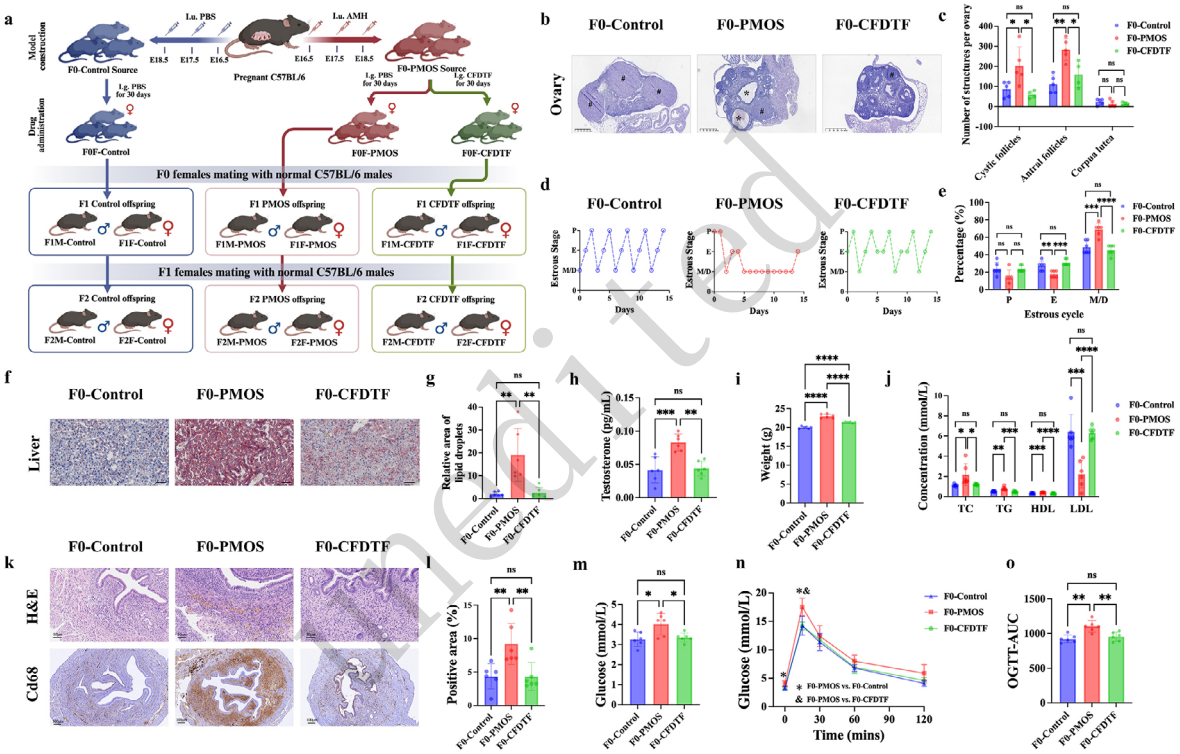



**Fig. 1 CFDTF's effects on the reproductive phenotypes of PMOS model mice. (a) The experimental design of the in vivo study. (b) The typical histological staining of ovaries in F0 mice; # represents corpora lutea and * represents cystic follicles; scale bar = 400 μm. (c) The number of cystic follicles, corpora lutea, and antral follicles per ovary of F0 mice. (d) and (e) The representative estrous cyclicity and statistical analysis of each stage over the 14-day monitoring period in three groups of founder-generation (F0) mice: P, proestrus; E, estrus; M, metestrus; D, diestrus. (f) and (g) Typical Oil Red O staining (scale bar = 50 μm) and the relative area of lipid droplets of the livers in F0 mice. (h) Serum testosterone in F0 mice at 6 months. (i) The weight of F0 mice at 6 months. (j) The serum levels of total cholesterol (TC), triglycerides (TG), high-density lipoprotein (HDL), and low-density lipoprotein (LDL) of F0 mice. (k) Typical H&E staining (scale bar = 50 μm) and immunohistochemical validation of *Cd68* (scale bar = 100 μm) in uterine tissues of F0 mice. (l) Quantification of the positive staining area in immunohistochemical analyses of Cd68 in F0 mice. (m) The fasting blood glucose levels of F0 mice. (n) The oral glucose tolerance test (OGTT) of F0 mice. (o) The comparison of the area under the curve (AUC) of the OGTT. Data represent mean ± standard deviation (SD), n = 5 – 6 per group, except (c), where n = 4 – 5 per group. Ns, non-significant, * $P < 0.05$, ** $P < 0.01$, **** $P < 0.0001$.**

## 3.2 The multigenerational effects of preconceptional CFDTF administration on the reproductive phenotypes of F1 and F2 offspring of the PMOS mouse model

Preconceptional CFDTF administration effectively restored normal estrous cyclicity (Figs. 2a and 2b) and further decreased testosterone levels in F1F-PMOS offspring (all $P<0.05$; Fig. 2e). However, estrous cyclicity in F2F offspring was comparable among the three groups (Figs. 2c and 2d), and the elevated serum testosterone levels in F2F-PMOS only exhibited a non-significant decreasing trend following preconceptional CFDTF administration ($P=0.0517$; Fig. 2g). Histologically, in F1 and F2 female offspring, preconceptional CFDTF administration significantly decreased the number of cystic follicles, and the number of antral follicles also showed a decreasing trend (F1F: $P=0.1640$; F2F: $P=0.8642$; Figs. 2f and 2h). The corpora lutea remained comparable among the three groups (Figs. 2f, 2i, 2h and 2j). Inflammatory infiltration in the myometrium was observed in the uterine tissues of both F1F- and F2F-PMOS mice; these inflammatory lesions were markedly attenuated following preconceptional administration of CFDTF (Figs. 2k and 2l). In F1F offspring, *Cd68* immunostaining showed a non-significant increasing trend in the PMOS group ($P=0.0870$; Fig. 2m), while the F1F-CFDTF group exhibited significantly lower Cd68-positive infiltration than the PMOS group that was comparable to that of controls (Fig. 2m). In F2F offspring, Cd68 positivity did not differ significantly among the three groups (Fig. 2p).

For the male offspring, CFDTF decreased the elevated testosterone levels in F1M-PMOS mice (Fig. 2n). Histologically, the F1M-PMOS group showed a significantly higher incidence of abnormal seminiferous tubules, and this pathological feature was substantially rescued by preconceptional CFDTF administration in F0 (Figs. 2o and 2s); however, these differences were less pronounced in the F2 male offspring (Figs. 2q, 2r, and 2t).

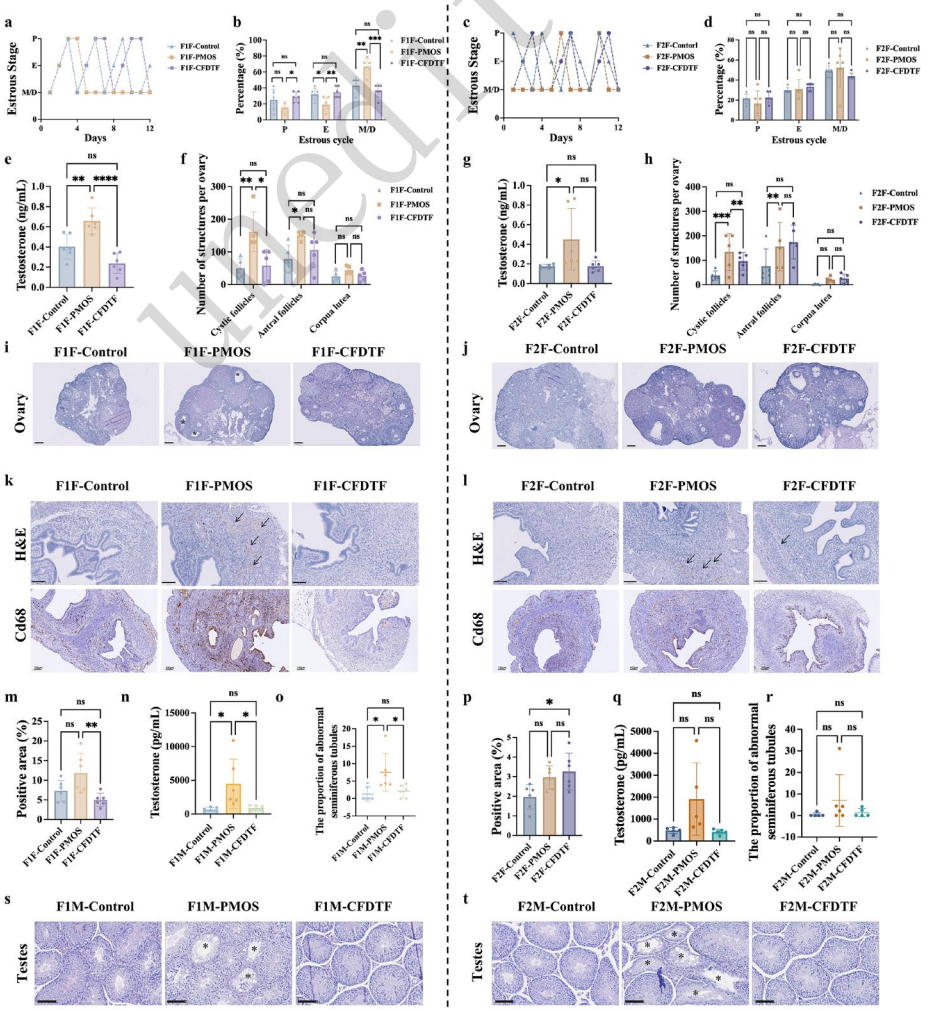


**Fig. 2 The multigenerational effects of preconceptional CFDTF administration on the reproductive phenotypes of F1 and F2 offspring of the PMOS mouse model. (a) and (c) Representative estrous cyclicity of first-generation (F1F) and second-generation female (F2F) offspring: P, proestrus; E, estrus; M, metestrus; D, diestrus. (b) and (d) The statistical analysis of each stage over the 14-day monitoring period in three groups of F1F and F2F offspring. (e) and (g) The serum testosterone levels of F1F and F2F offspring. (f) and (h) The number of cystic follicles, corpora lutea and antral follicles per ovary of F1F and F2F offspring. (i) and (j) Typical H&E staining of the ovaries of F1F and F2F offspring; scale bar = 100 μm. (k) and (l) Typical H&E staining and immunohistochemical validation of Cd68 in uterine tissues of F1F and F2F offspring; scale bar = 100 μm, arrow shows the inflammatory lesion. (m) and (p) Quantification of the positive staining area in immunohistochemical analyses of *Cd68* in F1F and F2F offspring. (n) and (q) Serum testosterone levels of first-generation (F1M) and second-generation male (F2M) offspring at 6 months. (o) and (r) Proportion of abnormal seminiferous tubules in F1M and F2M offspring. (s) and (t) Typical H&E staining of testicular tissues in F1M and F2M offspring; scale bar = 100 μm. Data represent mean ± standard deviation (SD), n = 5 − 6 per group. Ns, non-significant, * $P < 0.05$, ** $P < 0.01$, **** $P < 0.0001$.**

### 3.3 Multigenerational effects of preconceptional CFDTF administration on the glucolipid metabolism of F1 and F2 female offspring of the PMOS mouse model

Preconceptional CFDTF administration in F0 effectively mitigated glucolipid metabolic disturbances in female offspring. For glucose metabolism, preconceptional CFDTF administration in F0 significantly decreased the fasting blood glucose levels in F1F- and F2F-PMOS group (all $P<0.001$, Figs. 3a and 3d). The OGTT remained comparable across the three groups of F1 female offspring ($\varepsilon=0.5550$ for F1F and $\varepsilon=0.4502$ for F2F; Figs. 3b and 3e), and the F2F-PMOS group showed significantly higher glucose tolerance than the F2F-Control mice (Figs. 3c and 3f).

Regarding lipid metabolism, preconceptional CFDTF intervention markedly attenuated the endpoint body weight gain in F1F-PMOS mice (all $P<0.01$; Fig. S2a), but the weight change remained comparable among the three groups in F2F offspring ($\varepsilon = 0.3151$ for F2F, Figs. S2b-c). CFDTF administration significantly suppressed the abnormally elevated levels of TG, LDL and TBA in F1F-PMOS offspring (all $P < 0.05$; Figs. 3g-h), but HDL and DBIL levels were not restored by CFDTF and differed between the PMOS and CFDTF conditions in F1F mice (Figs. 3g-h). In F2F mice, the metabolic phenotype was less extensive: LDL levels were significantly reduced by CFDTF treatment (Fig. 3i), whereas the levels of TBA, TBIL, and DBIL remained comparable among groups in F2F (Fig. 3j). Histologically, preconceptional CFDTF administration significantly reversed the larger subcutaneous adipocytes in both F1F- and F2F-PMOS mice (Figs. 3k-l) and prevented the hepatic lipid deposition observed in F1F-PMOS mice, with a similar but statistically non-significant trend in F2F-PMOS mice ($P = 0.2930$; Figs. 3m-n).

Unedited

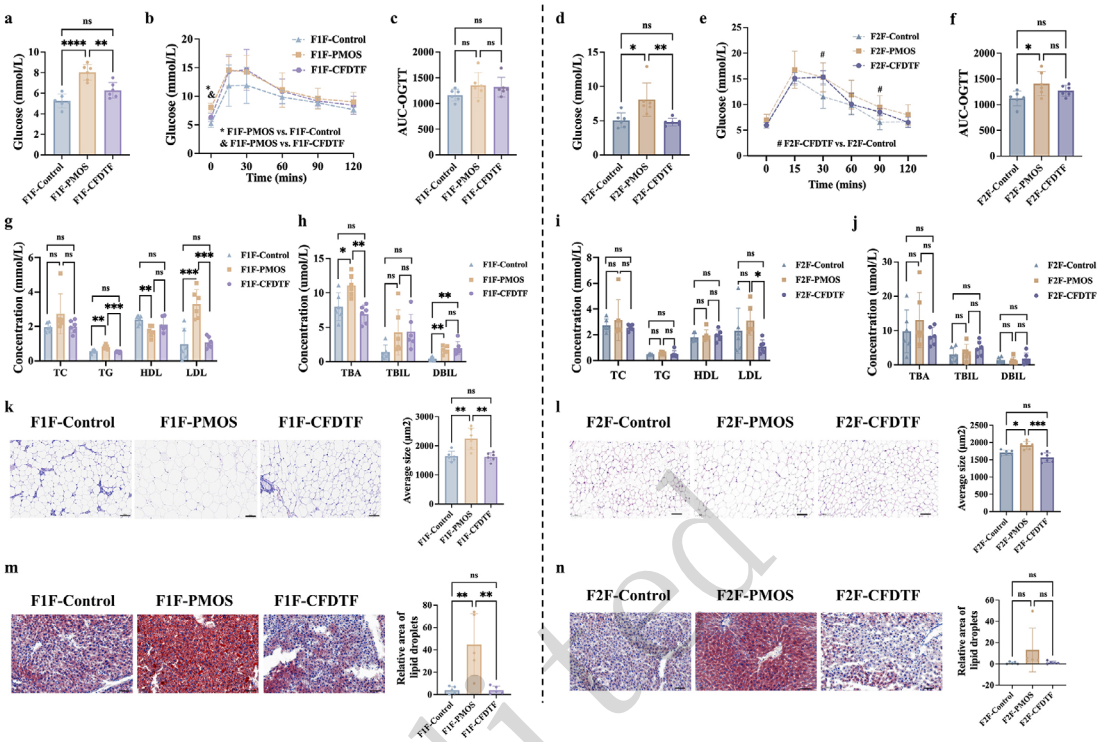



**Fig. 3 The multigenerational effects of preconceptional CFDTF administration on the glucolipid metabolism of F1 and F2 female offspring of the PMOS mouse model. (a) and (d) Fasting blood glucose levels in the first-generation (F1F) and second-generation female (F2F) offspring. (b) and (e) Oral glucose tolerance test (OGTT) of F1F and F2F offspring. (c) and (f) Comparison of the area under the curve (AUC) of the OGTT. (g) and (i) Serum levels of total cholesterol (TC), triglycerides (TG), high-density lipoprotein (HDL), and low-density lipoprotein (LDL) of F1F and F2F offspring. (h) and (j) Serum levels of total bile acid (TBA), total bilirubin (TBIL), and direct bilirubin (DBIL) of F1F and F2F offspring. (k) and (l) Typical H&E staining of the subcutaneous adipose tissues and the average size of adipocytes of F1F and F2F offspring; scale bar = 50 μm. (m) and (n) Typical Oil Red O staining and the relative area of lipid droplets of the livers in F1F and F2F offspring; scale bar = 50 μm. Data represent mean ± standard deviation (SD), n = 5 − 6 per group. Ns, non-significant, * $P < 0.05$, ** $P < 0.01$, *** $P < 0.001$, **** $P < 0.0001$.**

Unedited

### 3.4 Multigenerational effects of preconceptional CFDTF administration on the glucolipid metabolism of the F1 and F2 male offspring of the PMOS mouse model

For male offspring, preconceptional CFDTF intervention tended to attenuate the endpoint body weight gain in F1M-PMOS mice ($P = 0.0658$; Fig. S2d), and significantly reduced 6-month and 9-week body weight in F2M-PMOS mice (all $P < 0.05$; $\varepsilon = 0.6888$; Figs. S2e-f). The glucose metabolism analysis showed that preconceptional CFDTF administration significantly decreased the higher fasting blood glucose levels in F1M- and F2M-PMOS mice (Fig. 4a), while the OGTT revealed a relatively higher glucose tolerance among F1M-PMOS mice ($\varepsilon = 0.7539$ for F1M and $\varepsilon = 0.6447$ for F2M; Figs. 4b-c). In F2M offspring, preconceptional CFDTF administration significantly reduced fasting blood glucose levels as well as abnormal glucose tolerance in F2M-PMOS mice (Figs. 4d-f). For lipid metabolism, CFDTF significantly suppressed the elevated levels of TC and LDL in the F1M-PMOS mice (Fig. 4g) and significantly decreased the number of hepatic lipid droplets in both F1M-PMOS and F2M-PMOS mice (Figs. 4m-n), whereas no significant differences in TC or LDL levels were observed among the three F2M groups (Fig. 4i). Serum markers of hepatic function and biliary excretion, including TBA, TBIL and DBIL, remained comparable among the groups of F1 and F2 male mice (Figs. 4h and 4j). Furthermore, the average area of subcutaneous adipocytes was comparable among the three groups of F1M and F2M offspring (Figs. 4k-l).

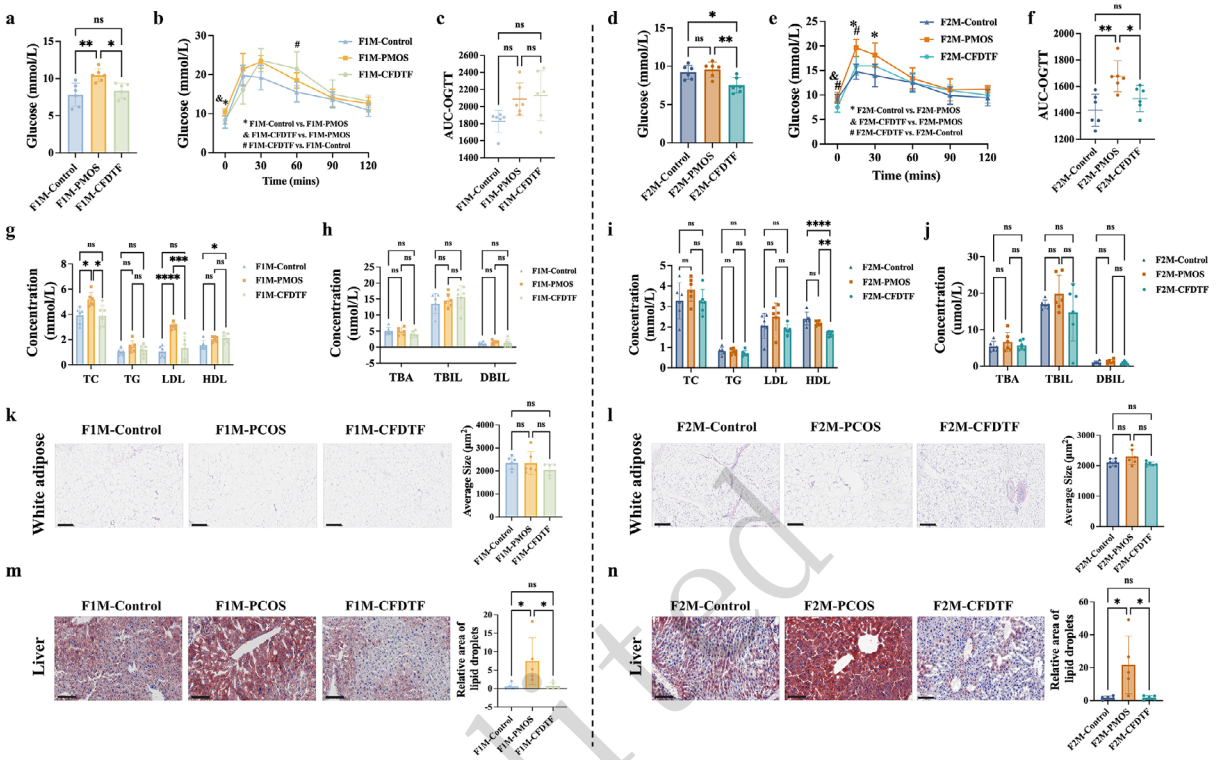



**Fig. 4 The multigenerational effects of preconceptional CFDTF administration on glucolipid metabolism of the F1 and F2 male offspring of the PMOS mouse model. (a) and (d) Fasting blood glucose levels of first-generation (F1M) and second-generation male (F2M) offspring. (b) and (e) Oral glucose tolerance test (OGTT) of F1M and F2M offspring. (c) and (f) Comparison of the area under the curve (AUC) of the OGTT. (g) and (i) Serum levels of total cholesterol (TC), triglycerides (TG), high-density lipoprotein (HDL), and low-density lipoprotein (LDL) of F1M and F2M offspring. (h) and (j) Serum levels of total bile acid (TBA), total bilirubin (TBIL), and direct bilirubin (DBIL) of F1M and F2M offspring. (k) and (l) Typical H&E staining of the white adipose tissue and the average size of adipocytes of F1M and F2M offspring; scale bar = 200 μm. (m) and (n) Typical Oil Red O staining and the relative area of lipid droplets of the livers in F1M and F2M offspring; scale bar = 100 μm. Data represent mean ± standard deviation (SD), n = 6 per group, except (m) and (n), where n = 5 per group. Ns, non-significant, * $P < 0.05$, ** $P < 0.01$, *** $P < 0.001$, **** $P < 0.0001$**

### 3.5 Reshaping of conserved IFN-driven inflammatory activation by preconceptional CFDTF administration across three generations of the PMOS mouse model

We found that preconceptional CFDTF administration significantly attenuated inflammatory infiltration in the uterine tissues of both F1F- and F2F-PMOS mice (Figs. 2k and 2l). To explore the mechanisms underlying the effects of CFDTF on the offspring of PMOS and to ensure cross-generational comparability, uterine tissues were collected from consistent anatomical sites and at approximately 25 weeks and diestrus stages across all three generations, providing a rigorous foundation for transcriptomic comparison (Fig. 5a).

GSVA-based principal component analysis (PCA) revealed that while the expression landscapes of the three groups exhibited considerable overlap in the F0F and F1F offspring, a clearer separation emerged in F2F, where preconceptional CFDTF administration shifted from the PMOS cluster toward the control (Figs. 5b-d). At the phenotype level, GSEA identified IFN-α and IFN-γ responses as the hallmarks most consistently reversed by preconceptional CFDTF administration in F0F and F1F, positioning IFN inflammatory signaling as a primary therapeutic target in PMOS uteri (Figs. 5e-f). In F2F, however, neither IFN hallmark was enriched; instead, allograft rejection, epithelial-mesenchymal transition and early estrogen response were identified as the predominant altered hallmarks, indicating a generational shift such as transcriptomic dysregulation (Fig. 5g). At the sample level, heatmap analysis showed that the significant elevation of both IFN hallmarks in PMOS model uteri was effectively reversed by preconceptional administration of CFDTF in F0. In F1F, the

Unedited

quantitative GSVA enrichment scores and IFN module scores remained significantly lower in the CFDTF group than in the PMOS group (Figs. 5k-l), suggesting that therapeutic imprinting of CFDTF is partially sustained across generations (Figs. 5h and 5i). Notably, F2F-PMOS uteri showed paradoxical suppression of IFN hallmark signaling, with F2F-CFDTF and F2F-Control groups having relatively higher IFN module scores (Figs. 5j and 5m). Taken together, these results established that the therapeutic effects of preconceptional CFDTF administration on PMOS-associated uterine inflammation are multigenerationally sustained through a conserved cytokine network, which is functionally linked to the IFN inflammatory axis.

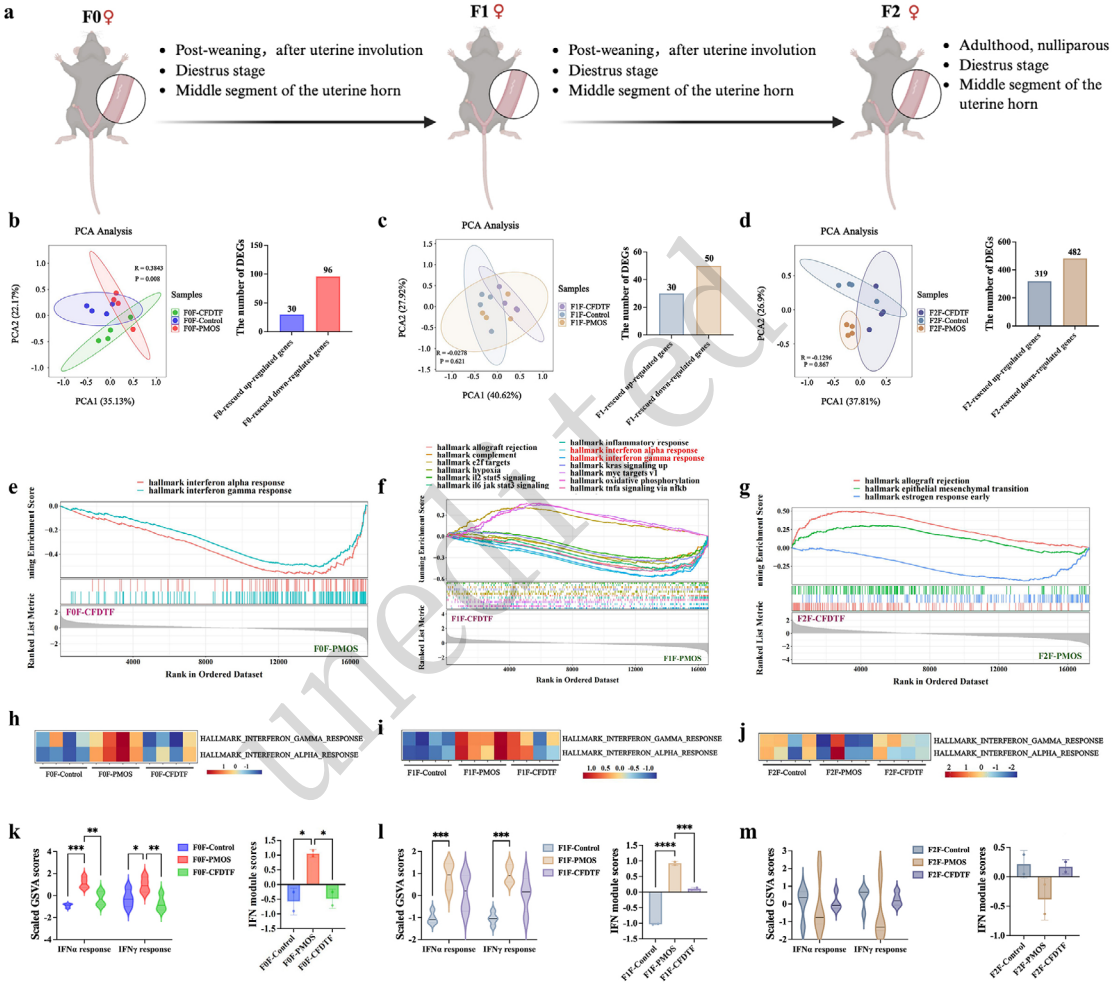



**Fig. 5. The preconceptional CFDTF administration reshapes conserved IFN-driven inflammatory activation across generations of the PMOS mouse model. (a) The workflow of the uterine tissue collection in three generations. Uterine samples of all three generations were collected at comparable adult ages of approximately 25 weeks (F0 and F1 post-weaning, after completed uterine involution; F2 nulliparous adults) from the middle segment of the uterine horn. (b-d) Principal component analysis (PCA) of gene set variation analysis (GSVA) scores and the number of up- or down-rescued differentially expressed genes (DEGs) in three generations. (e-g) Gene set enrichment analysis (GSEA) plots of significantly enriched rescued hallmark pathways of CFDTF in three generations. (h-j) Heatmap of GSVA enrichment scores of interferon (IFN) -related signaling pathways in three generations. (k-m) Violin plots showing the scaled GSVA scores for hallmark IFN-α response and hallmark IFN-γ response and the IFN module scores in three generations. Data represent mean ± standard deviation (SD), n = 4 per group. Ns, non-significant, * $P < 0.05$, ** $P < 0.01$, *** $P < 0.001$, **** $P < 0.0001$.**

### 3.6 Attenuation of inflammatory signaling and immune microenvironment remodeling by preconceptional CFDTF administration across generations

KEGG enrichment analysis of rescued DEGs consistently identified mmu05323—Rheumatoid Arthritis, mmu05321—Inflammatory Bowel Disease, and mmu04060—Cytokine-cytokine receptor interaction as

common top-enriched rescued pathways across all three generations (Figs. 6a-c), indicating that cytokine-driven inflammatory signaling is a stable target of CFDTF in alleviating uterine pathology associated with PMOS across generations. Immune cell infiltration analysis of uterine tissues revealed generation-dependent compositional changes, with the most prominent PMOS-associated immune dysregulations and their normalization by preconceptional CFDTF administration observed in the F2 generation (Figs. 6d-f, S3). In F0, the only significant difference among groups was a reduction in memory $CD8^+$ T cells in the F0F-PMOS group compared with the F0F-Control group ($P = 0.029$), which was not restored by CFDTF (Fig. 6d). In F1, eosinophils were reduced in the F1F-PMOS group compared with the F1F-Control group ($P = 0.020$), whereas M2 macrophages were significantly increased in the F1F-CFDTF group relative to both F1F-PMOS ($P = 0.002$) and F1F-Control ($P = 0.002$) groups, indicating a treatment-induced M2 shift rather than a reversal of the model effect (Fig. 6e). In F2, the F2F-PMOS group exhibited significantly increased memory B cells and M1 macrophages, together with reduced Th17 cells, monocytes, and resting NK cells, compared with the F2F-Control group (all $P < 0.05$). Preconceptional CFDTF administration shifted these alterations toward the Control-like direction: monocytes and resting NK cells were significantly restored, whereas memory $CD8^+$ T cells and naive $CD8^+$ T cells differed significantly between the F2F-CFDTF and F2F-PMOS groups. The shifts in memory B cells, M1 macrophages, and Th17 cells followed the same direction but did not reach statistical significance ($P = 0.1132$, $P = 0.3545$, and $P = 0.0513$, respectively). Eosinophils were specifically elevated in the F2F-CFDTF group relative to both F2F-PMOS ($P = 0.008$) and F2F-Control ($P = 0.011$) groups (Fig. 6f).

To evaluate the multigenerational impact of CFDTF, we integrated the scoring systems and immune profiles across F0F, F1F, and F2F. As shown in Fig. 6g, CFDTF effectively attenuated the marked inflammatory activation indicated by the high IFN score in the F0F generation. As IFN signaling in the PMOS group shifted from strong activation in F0F toward a potentially exhausted state in F2F, CFDTF maintained a consistent buffering effect across generations. Although the between-group difference gradually decreased, CFDTF still limited the transmitted inflammatory imprint and promoted IFN-related homeostasis by F2F (Fig. 6g). Consistent with this observation, the significance of the rescue scores in the CFDTF groups exhibited a gradual decline across generations, indicating that the extent of transcriptomic normalization diminished from F0F to F2F (Fig. 6h). The robustness of these findings was confirmed by sensitivity analyses using four more stringent rescue-gene definitions (e.g., $\geq 50\%$ or complete restoration toward control levels); the rescue scores remained significantly higher in the CFDTF group under all criteria, and hub-gene identification was largely unaffected (Table S3). We then compared immune cell populations showing significant alterations in each generation across generations (Fig. 6i). Consistent with the generation-specific pattern observed at the transcript level, no immune cell population was significantly altered in all three generations. Memory $CD8^+$ T cells came closest, as they were significantly affected in every generation, but in different directions and contrasts—reduced in F0F-PMOS and in F1F-CFDTF, yet restored by CFDTF in F2. Memory B cells showed opposite directions across generations (numerically lower in F0- and F1-PMOS, but significantly increased in F2-PMOS), and eosinophils were altered in both F1 and F2 but in different contexts (reduced by PMOS in F1; elevated by CFDTF in F2). Overall, immune dysregulation under PMOS conditions was sparse in F0, largely treatment-induced in F1, and broadest in F2, where preconceptional CFDTF administration also achieved the most extensive normalization.

Uncorrected

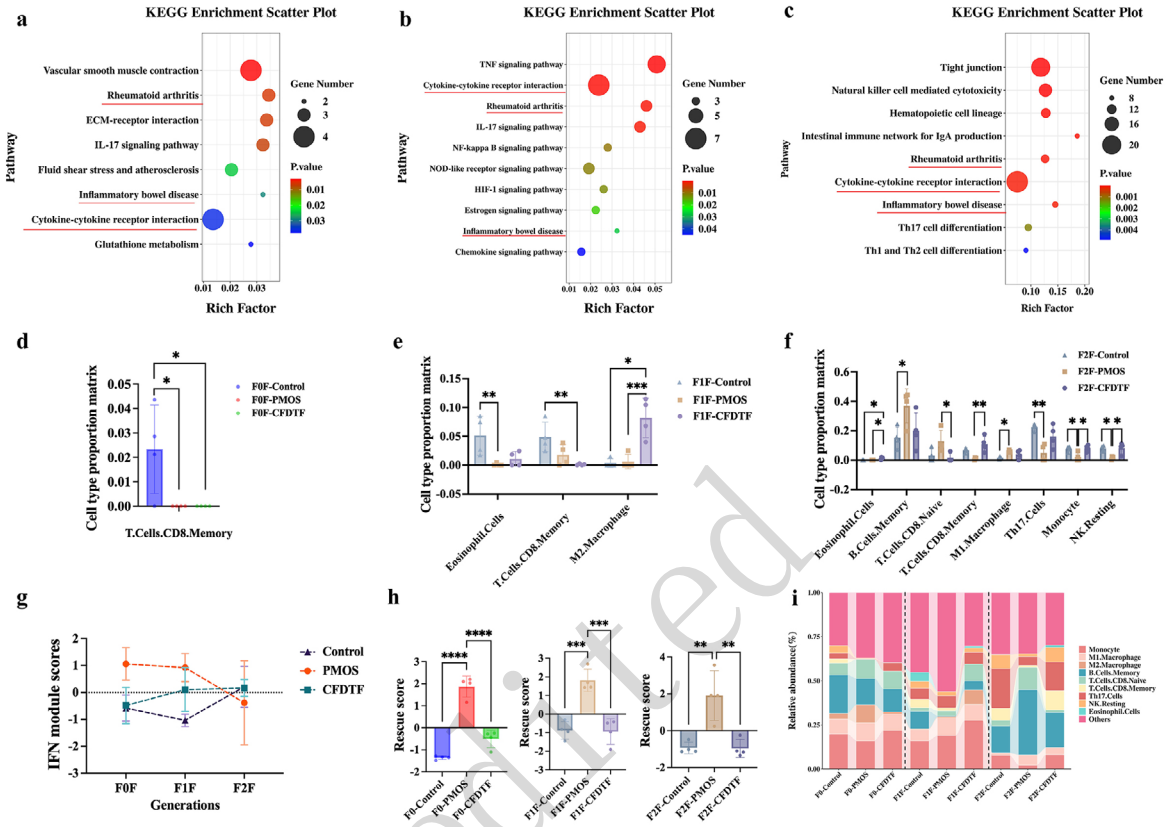



**Fig. 6 Preconceptional CFDTF administration attenuates inflammatory signaling and immune microenvironment remodeling across generations. (a-c) Kyoto Encyclopedia of Genes and Genomes (KEGG) pathway enrichment of rescued differentially expressed genes (DEGs) across three generations; the red line indicates the common pathway. (d-f) Significantly changed cell types in immune cell infiltration analysis using ImmuCellAI-mouse across three generations. (g) Changes in the interferon (IFN) module scores across three generations. (h) Changes in DEGs' rescue scores across three generations. (i) Stacked bar chart of uterine immune cell composition estimated by ImmuCellAI-mouse; cell populations showing significant differences in at least one generation are displayed individually, and all remaining populations are merged as 'Others'. n = 4 per group. * $P < 0.05$, ** $P < 0.01$, *** $P < 0.001$, **** $P < 0.0001$.**

Unedited

### 3.7 Identification of multigenerational inflammatory hub genes modulated by the preconceptional CFDTF administration

No common DEGs were identified across the three generations (Table S4). There were 12 hub rescue genes in F0F, 11 in F1F, and 19 in F2F; furthermore, hub rescue genes were shared across the generations (Table S5 and Figs. 7a-c). We then further filtered 11 candidate genes based on significant correlation with the IFN module score (Figs. 7a-c and Table S6), supporting functional coupling between rescue-associated transcriptional remodeling and interferon-related immune activation. In F0F, *Tnf*, *Il17a*, *A2m*, and *Ly6g* were significantly positively associated with IFN-score, while *Arg2* was negatively related to IFN-score (Figs. 7a). In F1F, *Il1a*, *Ptgs2, Nos2*, *Cxcl2*, *Lif*, and *Bmal1* were significantly positively associated with IFN-score and *Ccl2* was negatively associated with IFN-score (Fig. 7b). In F2F, *Tyrobp*, *Fcgr3*, *Ccl5*, *Fcer1g*, *Cd74*, *Tgfb1*, and *Ctss* were significantly positively associated with IFN-score (Fig. 7c). Among these, *Tnf* and *Il17a* overlapped with hub genes in F0F, *Il1a* in F1F, and *Tgfb1* in F2F. Notably, *Tnf*, *Il17a*, *Il1a* and *Tgfb1* showed a significant positive correlation with the IFN score (Table S5 and Figs. 7a-c).

To validate the transcriptomically nominated candidate genes at the tissue level, immunohistochemical analyses of *Il1a*, *Il17a*, *Tnf*, and *Tgfb1* in the uterine tissues of the three generations were performed (Figs. 7d-f), complemented by RT-qPCR quantification of the same genes (Figs. 7j-l). At the protein level, *Il17a* was

significantly upregulated in both F0- and F1-PMOS uteri compared with the corresponding controls, and these elevations were significantly attenuated by preconceptional CFDTF administration (Figs. 7g-h). *Il1a* did not differ significantly between the PMOS and Control groups in either generation, although its expression was significantly lower in F0-CFDTF than in F0-PMOS (Fig. 7g). *Tnf* and *Tgfb1* immunostaining showed no significant group differences in any generation, and none of the four markers differed significantly among groups in F2 (Fig. 7i). At the mRNA level (Figs. 7j-l), the transcriptomic predictions were broadly confirmed: *Il1a*, *Il17a*, and *Tgfb1* were significantly upregulated in the PMOS groups of all three generations and reversed toward control levels by CFDTF, with *Tnf* exhibiting the same pattern in F1 and F2. Notably, *Il1a* exhibited distinct spatial patterns across generations, being diffusely distributed across uterine layers in F0- and F1-PMOS but confined to the endometrial layer in F2-PMOS (Figs. 7d-f). These findings support generation-specific expression of candidate inflammatory genes and their potential roles as mediators of IFN-associated uterine inflammation across generations, although weaker protein-level concordance in F2 suggests post-transcriptional regulation or limited sensitivity of immunohistochemical quantification, and causal roles remain to be established by functional experiments.

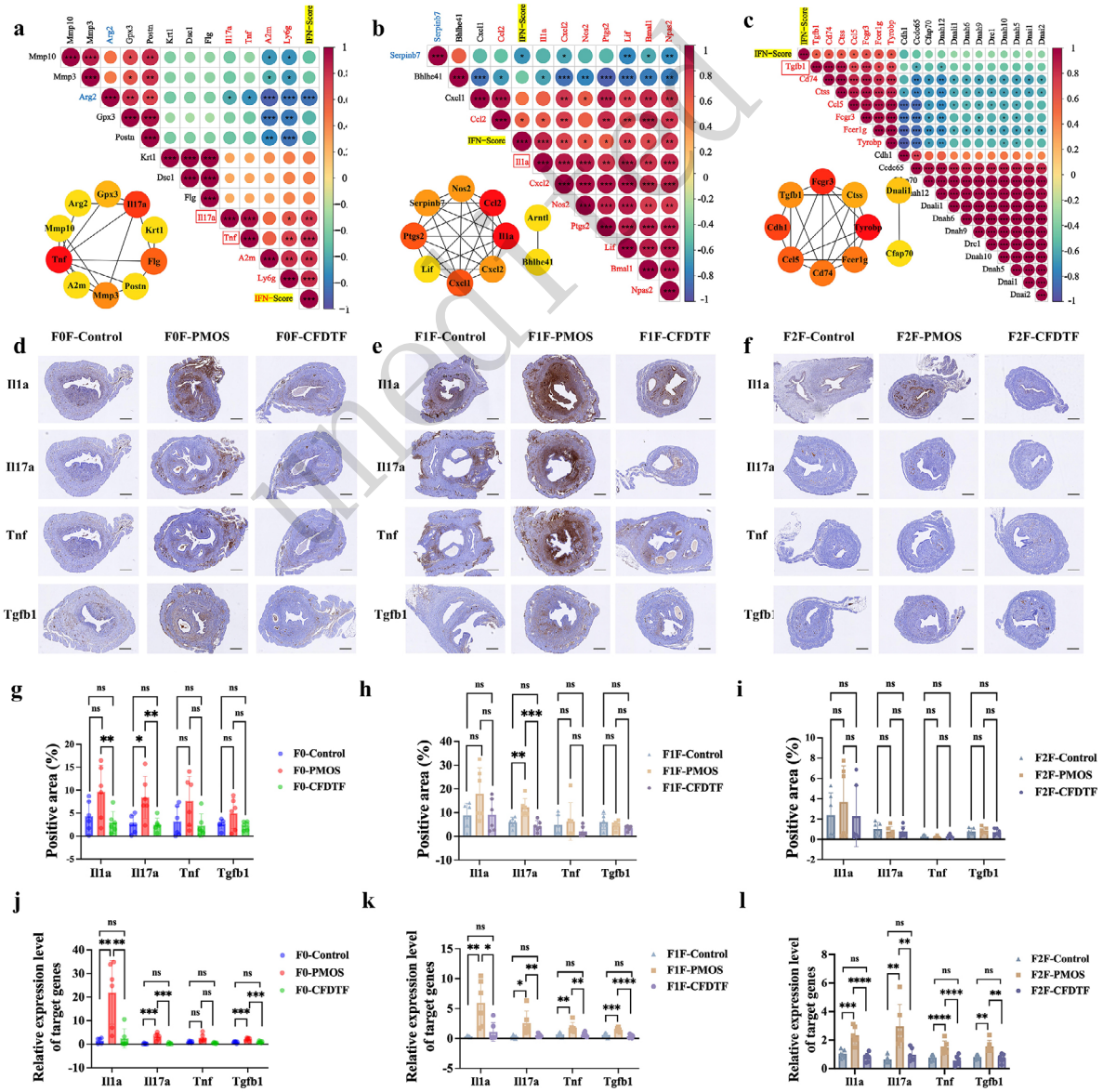



**Fig. 7 Cross-generational convergence of protein-protein interaction (PPI) networks and immunohistochemical valida-**

**tion in uterine tissues across three generations. (a-c) Correlation analyses with the interferon (IFN) score and hub genes across three generations were identified based on the PPI networks. The circle-PPI network represents the "Degree" levels; the darker the nodes, the more important the gene. Blue text represents a negative correlation with the gene and IFN-score, while red text represents a positive correlation. The boxed items highlight the candidate genes identified after the final intersection analysis. (d-f) Immunohistochemical validation of *Il1a*, *Il17a*, *Tnf* and *Tgfb1* in uterine tissues across three generations. Consecutive sections from the same uterus were stained with different antibodies; scale bar = 200μm. (g-i) Quantification of the positive staining area in immunohistochemical analyses across three generations, n = 5 per group. (j-l) Relative expression levels of target genes in uterine tissues across three generations based on quantitative real-time PCR (RT-qPCR), n = 6 per group. Ns, non-significant, * $P < 0.05$, ** $P < 0.01$, *** $P < 0.001$, **** $P < 0.0001$.**

## 4 Discussion

Chronic low-grade inflammation is increasingly recognized as a key contributor to PMOS pathogenesis and is closely associated with insulin resistance, ovarian dysfunction, and metabolic disturbance (Deng et al., 2024; Liu et al., 2024). Sustained uterine inflammatory activation may disrupt endometrial structure and function, impair embryo implantation, and alter the intrauterine environment, thereby influencing offspring developmental programming (Aboeldalyl et al., 2021; Stener-Victorin and Deng, 2021; Deng, et al., 2024). Persistent uterine inflammation may therefore represent a biological link between maternal PMOS status and adverse reproductive or metabolic outcomes in descendants. In the present study, we found that preconceptional CFDTF administration attenuated PMOS-associated uterine inflammatory phenotypes, with generation-dependent patterns. Therefore, reduced inflammatory infiltration and improved uterine pathology in offspring suggest that CFDTF may interrupt PMOS multigenerational transmission, at least in part, by reshaping the uterine inflammatory microenvironment.

Before turning to the uterine mechanism, it is worth noting that the reproductive phenotypes themselves showed generation-dependent patterns. The accumulation of antral and cystic follicles observed in F0, F1F, and F2F is consistent with the disrupted folliculogenesis reported in PAMH and other PMOS-like models (Tata, et al., 2018), in which altered follicle-stage distribution rather than true follicular cysts is the predominant histological feature. However, this morphological phenotype was only partially reversed: cystic follicle numbers were significantly reduced in both generations, whereas antral follicle accumulation persisted and corpora lutea numbers were comparable among groups. The offspring ovary's follicular pool is programmed during fetal and early postnatal development (Smith et al., 2009; Findlay et al., 2015) and may thus be less amenable to a preconceptional intervention than functional readouts, which remain plastic in adulthood (Mimouni et al., 2021). The benefits of preconceptional CFDTF administration are thus reflected primarily by functional and inflammatory improvements rather than by complete normalization of ovarian morphology. Uterine Cd68 quantification revealed a generation-dependent pattern of low-grade inflammation: a significant increase in the directly exposed F0 generation, an intermediate, non-significant increase in F1F offspring, and no detectable difference in F2F offspring. This graded attenuation parallels the transgenerational attenuation of the reproductive and metabolic phenotypes described above. In F1F offspring, the significantly lower Cd68 positivity in the CFDTF group relative to the PMOS group, in the absence of a significant Control-PMOS difference (P = 0.0870), should be interpreted as a partial normalizing trend rather than rescue of a fully penetrant inflammatory phenotype; importantly, Cd68 levels in CFDTF-treated offspring did not differ from those of controls, indicating that the intervention did not suppress basal uterine immune surveillance. Notably, although uterine samples from the three generations were collected at comparable adult ages, F0 and F1 females were parous (post-weaning) whereas F2 females were nulliparous. Given that parity can influence endometrial morphology and uterine immune cell content, uterine comparisons were restricted to within-generation groups, and cross-generational patterns should be interpreted with caution.

Within this generation-dependent phenotype gradient, estrous cyclicity changed most markedly. F0 and F1F-PMOS mice displayed disrupted cycles, whereas the three F2F groups exhibited comparable cyclicity. Notably, F2F-PMOS mice still retained persistent reproductive, metabolic, and uterine inflammatory abnormalities. Our observations diverge from those of Mimouni et al., who reported sustained estrous cycle disruption in PAMH F2 females (Mimouni, et al., 2021). Two methodological differences may explain this inconsistency. First, their cyclicity assessments relied on larger sample sizes (n = 12–19, compared with n = 6 in our study). Second, the estrous cycle monitoring window differed modestly, as they recorded cycles for 16 consecutive days across P60–P90, whereas our monitoring spanned 14 days starting at P70. We cannot rule out

under review

faint residual cycle changes that fall beneath the detection threshold of our animal cohort. Biologically, phenotypes transmitted exclusively via the F1 germline tend to weaken with successive generations. As a functional readout of the hypothalamic–pituitary–ovarian axis, estrous cyclicity may recover sooner than ovarian structural or metabolic phenotypes.

Beyond the reproductive axis, the metabolic alterations differed between F1F and F2F offspring, suggesting a generation dependent pattern rather than complete phenotypic replication. In F1F offspring, PMOS exposure increased TG, LDL, and TBA levels, whereas these alterations were largely attenuated in F2F. Notably, the elevated TBA in F1F-PMOS offspring was corrected by preconceptional CFDTF administration, while the LDL phenotype persisted into the F2F generation and remained amenable to CFDTF correction. This generation-dependent attenuation and remodeling of programmed traits is consistent with reports that molecular and metabolic outcomes of prenatal androgen or AMH exposure vary across generations rather than being identically reproduced (Risal, et al., 2019; Mimouni, et al., 2021). The generation specific elevation of TBA further suggests that bile acid homeostasis may contribute to the metabolic programming of PMOS offspring: bile acid metabolism is closely linked to PCOS pathophysiology (Qi et al., 2019), and an adverse maternal metabolic environment can disrupt offspring bile acid homeostasis and hepatic lipid metabolism (Thompson et al., 2022). However, because we measured only total bile acids, without profiling individual bile acid species or regulatory pathways, we cannot resolve the underlying mechanism here. The more pronounced effects of CFDTF in F1F offspring may reflect modification of the maternal endocrine-metabolic environment before conception (Risal, et al., 2019), thereby altering developmental programming of the directly exposed F1 generation, whereas the limited effects in F2F likely reflect partial attenuation of the programmed phenotype. This is consistent with previous studies showing that CFDTF ameliorates lipid and metabolic abnormalities in PCOS models (Yi, et al., 2021; Liu, et al., 2022), although the precise mechanisms remain incompletely defined. Interestingly, while impaired glucose tolerance was not observed in F1F offspring, it emerged in the F2F generation. Generation-specific manifestation of metabolic phenotypes has also been reported in prenatal androgen and PAMH models (Risal, et al., 2019; Mimouni and Giacobini, 2021). One possible explanation is that direct in utero exposure in F1 offspring elicits compensatory developmental adaptations that preserve glucose tolerance, whereas in F2 offspring—which are never directly exposed—germline-transmitted programming may selectively affect glucose homeostasis. Alternatively, a subtler F1F phenotype may have been below the detection limit of the present sample size.

To explore the molecular basis of these generation-dependent phenotypes, we performed transcriptomic sequencing on uterine tissues from F0F, F1F, and F2F offspring. Interestingly, no common rescue DEGs were identified across the three generations; however, GSEA and GSVA enrichment analyses revealed that hallmark IFN-α/γ responses were commonly rescued by preconceptional CFDTF administration in uterine transcriptomes across all three generations. Meanwhile, KEGG enrichment analysis of rescue DEGs consistently revealed convergence on a shared set of cytokine-driven inflammatory signaling across generations, and the genes shared by the three KEGG pathways were significantly correlated with the IFN module score, supporting a functional coupling between rescue-associated transcriptional remodeling and IFN-related immune activation. We obtained these mechanistic data exclusively from female uterine tissue; the sex specificity of the proposed mechanism is addressed in the discussion of the limitations below.

The observed "positive-to-negative" shift in the IFN module score in the PMOS group across generations supports the dynamic nature of multigenerational immune programming. The high IFN module score in F0F-PMOS reflects the immediate inflammatory stress induced by the PMOS-like environment, while the negative score in F2F-PMOS may reflect a compensatory dampening of the uterine immune responsiveness following ancestral stress, potentially through epigenetic mechanisms (Heard and Martienssen, 2014). The reduced differences in inflammatory levels among the Control, CFDTF, and PMOS groups in F2F offspring suggest less divergence in inflammatory phenotypes in later generations. However, the mechanisms underlying this observation remain unclear. Given the limited evidence for spontaneous resolution of PMOS-associated uterine inflammation across generations, these findings cannot determine whether reduced divergence results from attenuated transmitted traits, a persistent effect of CFDTF intervention, or both (Risal, et al., 2019; Luyckx et al., 2025). Further longitudinal analyses of uterine inflammatory and histopathological changes are needed to clarify these mechanisms

Collectively, these findings suggest that CFDTF's multigenerational rescue effects are mediated by restoring a common pathway-level regulatory program rather than by identical effector genes (Yin et al., 2025).

Under Peer Review

This aligns with the understanding that PMOS transmission involves complex epigenetic developmental programming rather than isolated molecular events (Stener-Victorin and Deng, 2025). This network-level mechanism explains how consistent pathological phenotypes persist across generations despite shifting gene expression profiles, suggesting that targeting conserved inflammatory pathways is a promising strategy for preventing multigenerational uterine inflammation (Deng, et al., 2024; De Robles et al., 2025).

Building on this pathway-level understanding, we next identified the candidate molecular mediators within these conserved programs for each generation: *Tnf* and *Il17a* in F0F, *Il1a* in F1F, and *Tgfb1* in F2F. *Tnf* and *Il1a* are classical pro-inflammatory cytokines involved in innate immune activation and inflammatory amplification, whereas *Il17a* is a key Th17-related effector cytokine that promotes cytokine and chemokine production, immune-cell recruitment, and tissue inflammatory remodeling (Turner et al., 2014; Huangfu et al., 2023; Mills, 2023). *Tgfb1* plays pleiotropic roles in immune regulation, tissue remodeling, and Treg/Th17 balance (Massague and Sheppard, 2023; Wang et al., 2023). The coordinated alterations in these molecules, along with transcriptomic enrichment of inflammatory pathways and pathological evidence of uterine inflammation, suggest that a network of innate and adaptive immune responses, rather than a single inflammatory mediator, may drive the mechanisms underlying CFDTF's multigenerational effects on PMOS-associated uterine abnormalities.

At the cellular level, ImmuCellAI-mouse analysis further revealed that uterine immune dysregulation was itself generation-dependent: sparse in F0, largely treatment-induced in F1, and broadest in F2, where preconceptional CFDTF administration also achieved the most extensive normalization. There are two notable features of this pattern. First, memory $CD8^+$ T cells were the only population significantly altered in all three generations, albeit in different directions, mirroring the generation-specific organization observed at the transcript level. Second, the prominent M2 macrophage polarization in the F1-CFDTF group was treatment-induced rather than model-driven, suggesting that CFDTF may actively promote an anti-inflammatory uterine milieu instead of merely blocking the model effect. These findings support conceptualizing the uterus as an immune-regulated environment shaped by local inflammatory networks, a hallmark of PMOS pathology (Wang et al., 2021), and indicate that preconceptional CFDTF administration helps restore uterine immune homeostasis, with the most pronounced effects in the F2 generation.

Nevertheless, several limitations should be acknowledged. First, our investigation primarily focused on the reproductive and glucolipid metabolic systems, as these are the most frequently reported and phenotypically prominent areas of dysfunction in PMOS offspring. However, the systemic nature of PMOS suggests that CFDTF's effects on other domains of PMOS offspring must be explored to provide a more holistic understanding of its multigenerational benefits. Second, due to the lack of fresh tissue samples, we could not perform flow cytometry to complement our validation of immune cell infiltration. While transcriptomic deconvolution and histopathological evidence indicated significant immune remodeling, further work incorporating fresh-tissue-based quantification is required to confirm these cellular shifts more robustly. Third, any threshold-based definition of rescued genes involves a degree of arbitrariness; however, sensitivity analyses applying more stringent criteria, up to complete restoration toward Control levels, yielded consistent results, supporting the robustness of our conclusions to the choice of rescue definition. Fourth, the mechanisms underlying the multigenerational effects of CFDTF on the PMOS offspring remain at the pathway and association level: our transcriptomic, RT-qPCR, and immunohistochemical data demonstrate an association between CFDTF treatment, the interferon-centered hub genes (*Tnf*, *Il17a*, *Il1a*, and *Tgfb1*), and the uterine inflammatory phenotype but cannot establish causality. Additionally, the whole-uterus bulk RNA-seq analysis could not distinguish changes in immune cell composition from cell-intrinsic transcriptional regulation. The proposed IFN axis should be treated as a mechanistic hypothesis requiring validation through in vitro experiments, such as cytokine stimulation and hub-gene perturbation in endometrial epithelial or stromal cell models, along with single-cell analysis and functional proteomics. Fifth, we performed all mechanistic investigations exclusively in female uterine tissue, so we cannot infer from the present data whether the benefits observed in male offspring are mediated by the same mechanism. As the uterus constitutes the intrauterine environment for both sexes, uterine improvements may contribute to male phenotypes via the maternal gestational milieu, a hypothesis requiring validation in gestational uterine/placental and male offspring tissues. Sixth, because litters per group were limited, we treated offspring rather than litters as the experimental unit; therefore, residual litter effects cannot be fully excluded. Future studies should increase litter numbers and model litter as a random effect. Seventh, we recorded body weight only at the experimental endpoint for the F1 generation. For

Under Peer Review

the F2 cohort, we also. Monitored body weight weekly from 3 to 10 weeks of age alongside endpoint weight measurement. Therefore, body weight data from these two generations cannot be directly compared. Finally, we did not formally assess fertility using a dedicated continuous-mating design, and this should be addressed in future work.

## 5 Conclusions

Preconceptional CFDTF administration effectively attenuated PMOS-like reproductive and metabolic abnormalities across generations by alleviating uterine inflammation.

### Data availability statement

The raw RNA-seq data generated in this study have been deposited in the NCBI Gene Expression Omnibus (GEO) database under accession number GSE334801. The dataset is currently under controlled access during the peer-review process and will be made publicly available upon publication of the article. Reviewer access can be provided upon request.

### Acknowledgments

We sincerely acknowledge the staff members of the Zhejiang Key Laboratory of Maternal and Infant Health for their dedicated technical support, meticulous maintenance of experimental equipment, and efficient administrative assistance throughout this study. Their professionalism and commitment were indispensable to the successful completion of our research. This study was supported by National Natural Science Foundation of China (No. 82374510 to J. Z.), National Key R&D Program of China (Grant no. 2024YFC3505800 to F.W.), the Health High-Level Talent Training Project (Innovative Talents), the Health Commission of Zhejiang Province, China (Grant no. [2021] 40 to F.Q.).

### Author contributions

Weihuan Hu performed the data curation and formal analysis, wrote the original draft, and visualised the figures. Meiping LI and Ningning XIE designed the methodology and visualised the figures. Fangfang WANG, Fan QU, and Jue ZHOU reviewed and edited the manuscript and acquired funding. Shaoyan YE, Siwen ZHANG, Wenshan ZENG and Bizhen WANG investigated and validated the experiments. Lu ZHAO edited the manuscript. Jue ZHOU conceptualised and supervised the study. All authors contributed to the scientific discussion of the data and manuscript and approved the final version.

### Compliance with ethics guidelines

Weihuan HU, Fangfang WANG, Meiping LI, Ningning XIE, Shaoyan YE, Siwen ZHANG, Wenshan ZENG, Bizhen WANG, Lu ZHAO, Fan QU, and Jue ZHOU declare that they have no conflicts of interest.

All procedures involving animals were approved by the Animal Ethics Committee of MSLT BIOTECH (Hangzhou) Co., Ltd. (Approval No. 2023H311106) and conducted in accordance with the ARRIVE 2.0 guidelines and with institutional and national guidelines for the care and use of laboratory animals.

### Declaration on the use of generative AI tools

During the preparation of this work, the authors used ChatGPT (OpenAI, GPT-5.5) to improve language and readability. After using this tool, the authors reviewed and edited the content as needed and take full responsibility for the content of the publication.

### References

Aboeldalyl S, James C, Seyam E, et al., 2021. The role of chronic inflammation in polycystic ovarian syndrome-a systematic review and meta-analysis. Int J Mol Sci, 22(5) https://doi.org/10.3390/ijms22052734

Banerjee S, Cooney LG, Stanic AK, 2023. Immune dysfunction in polycystic ovary syndrome. Immunohorizons, 7(5):323-332. https://doi.org/10.4049/immunohorizons.2200033

Byers SL, Wiles MV, Dunn SL, et al., 2012. Mouse estrous cycle identification tool and images. PLoS One, 7(4):e35538. https://doi.org/10.1371/journal.pone.0035538

Chin CH, Chen SH, Wu HH, et al., 2014. Cytohubba: Identifying hub objects and sub-networks from complex interactome. BMC Syst Biol, 8 Suppl 4(Suppl 4):S11. https://doi.org/10.1186/1752-0509-8-S4-S11

De Robles G, Wiggins KD, Del Mundo Z, et al., 2025. Unpacking pcos inflammation: From misconceptions to immune networks. Endocrinology, 166(12) https://doi.org/10.1210/endocr/bqaf166

Deng H, Chen Y, Xing J, et al., 2024. Systematic low-grade chronic inflammation and intrinsic mechanisms in polycystic ovary syndrome. Front Immunol, 15:1470283. https://doi.org/10.3389/fimmu.2024.1470283

Findlay JK, Hutt KJ, Hickey M, et al., 2015. How is the number of primordial follicles in the ovarian reserve established? Biol

Under review

Reprod, 93(5):111. https://doi.org/10.1095/biolreprod.115.133652
Foroutan M, Bhuva DD, Lyu R, et al., 2018. Single sample scoring of molecular phenotypes. BMC Bioinformatics, 19(1):404. https://doi.org/10.1186/s12859-018-2435-4
Hanzelmann S, Castelo R, Guinney J, 2013. Gsva: Gene set variation analysis for microarray and rna-seq data. BMC Bioinformatics, 14:7. https://doi.org/10.1186/1471-2105-14-7
Heard E, Martienssen RA, 2014. Transgenerational epigenetic inheritance: Myths and mechanisms. Cell, 157(1):95-109. https://doi.org/10.1016/j.cell.2014.02.045
Hu W, Xie N, Zhu H, et al., 2024. The effective compounds and mechanisms of cang-fu-dao-tan formula in treating polycystic ovary syndrome based on uplc/q-tof-ms/ms, network pharmacology and molecular experiments. J Pharm Biomed Anal, 239:115867. https://doi.org/10.1016/j.jpba.2023.115867
Huangfu L, Li R, Huang Y, et al., 2023. The il-17 family in diseases: From bench to bedside. Signal Transduct Target Ther, 8(1):402. https://doi.org/10.1038/s41392-023-01620-3
Liu L, Liu S, Bai F, et al., 2024. Investigating the role of inflammatory response in polycystic ovary syndrome using integrated rna-seq analysis. J Inflamm Res, 17:4701-4719. https://doi.org/10.2147/JIR.S460437
Liu S, Zhang Y, Yang F, et al., 2022. Modified cangfu daotan decoction ameliorates polycystic ovary syndrome with insulin resistance via nf-kappab/lcn-2 signaling pathway in inflammatory microenvironment. Front Endocrinol (Lausanne), 13:975724. https://doi.org/10.3389/fendo.2022.975724
Luyckx L, Myllykangas M, Saarela U, et al., 2025. Prenatally androgenized pcos mice have ovary-independent uterine dysfunction and placental inflammation aggravated by high-fat diet. Sci Adv, 11(19):eadu3699. https://doi.org/10.1126/sciadv.adu3699
Lyu F, Han F, Ge C, et al., 2023. Omicstudio: A composable bioinformatics cloud platform with real-time feedback that can generate high-quality graphs for publication. Imeta, 2(1):e85. https://doi.org/10.1002/imt2.85
Massague J, Sheppard D, 2023. Tgf-beta signaling in health and disease. Cell, 186(19):4007-4037. https://doi.org/10.1016/j.cell.2023.07.036
Miao YR, Xia M, Luo M, et al., 2022. Immucellai-mouse: A tool for comprehensive prediction of mouse immune cell abundance and immune microenvironment depiction. Bioinformatics, 38(3):785-791. https://doi.org/10.1093/bioinformatics/btab711
Mills KHG, 2023. Il-17 and il-17-producing cells in protection versus pathology. Nat Rev Immunol, 23(1):38-54. https://doi.org/10.1038/s41577-022-00746-9
Mimouni NEH, Giacobini P, 2021. Polycystic ovary syndrome mouse model by prenatal exposure to high anti-mullerian hormone. STAR Protoc, 2(3):100684. https://doi.org/10.1016/j.xpro.2021.100684
Mimouni NEH, Paiva I, Barbotin AL, et al., 2021. Polycystic ovary syndrome is transmitted via a transgenerational epigenetic process. Cell Metab, 33(3):513-530 e518. https://doi.org/10.1016/j.cmet.2021.01.004
Myers M, Britt KL, Wreford NG, et al., 2004. Methods for quantifying follicular numbers within the mouse ovary. Reproduction, 127(5):569-580. https://doi.org/10.1530/rep.1.00095
Nair AB, Jacob S, 2016. A simple practice guide for dose conversion between animals and human. J Basic Clin Pharm, 7(2):27-31. https://doi.org/10.4103/0976-0105.177703
Nakamoto T, Shiratsuchi A, Oda H, et al., 2004. Impaired spermatogenesis and male fertility defects in ciz/nmp4-disrupted mice. Genes Cells, 9(6):575-589. https://doi.org/10.1111/j.1356-9597.2004.00746.x
Newman AM, Liu CL, Green MR, et al., 2015. Robust enumeration of cell subsets from tissue expression profiles. Nat Methods, 12(5):453-457. https://doi.org/10.1038/nmeth.3337
Palomba S, Piltonen TT, Giudice LC, 2021. Endometrial function in women with polycystic ovary syndrome: A comprehensive review. Hum Reprod Update, 27(3):584-618. https://doi.org/10.1093/humupd/dmaa051
Park HR, Kim JH, Lee D, et al., 2019. Cangfu daotan decoction for polycystic ovary syndrome: A protocol of systematic review and meta-analysis. Medicine (Baltimore), 98(39):e17321. https://doi.org/10.1097/MD.0000000000017321
Percie Du Sert N, Hurst V, Ahluwalia A, et al., 2020. The arrive guidelines 2.0: Updated guidelines for reporting animal research. BMJ Open Sci, 4(1):e100115. https://doi.org/10.1136/bmjos-2020-100115
Qi X, Yun C, Sun L, et al., 2019. Gut microbiota-bile acid-interleukin-22 axis orchestrates polycystic ovary syndrome. Nat Med, 25(8):1225-1233. https://doi.org/10.1038/s41591-019-0509-0
Risal S, Pei Y, Lu H, et al., 2019. Prenatal androgen exposure and transgenerational susceptibility to polycystic ovary syndrome. Nat Med, 25(12):1894-1904. https://doi.org/10.1038/s41591-019-0666-1
Risal S, Manti M, Lu H, et al., 2021. Prenatal androgen exposure causes a sexually dimorphic transgenerational increase in offspring susceptibility to anxiety disorders. Transl Psychiatry, 11(1):45. https://doi.org/10.1038/s41398-020-01183-9
Smith P, Steckler TL, Veiga-Lopez A, et al., 2009. Developmental programming: Differential effects of prenatal testosterone and dihydrotestosterone on follicular recruitment, depletion of follicular reserve, and ovarian morphology in sheep. Biol Reprod, 80(4):726-736. https://doi.org/10.1095/biolreprod.108.072801
Stener-Victorin E, Deng Q, 2021. Epigenetic inheritance of polycystic ovary syndrome - challenges and opportunities for treatment. Nat Rev Endocrinol, 17(9):521-533. https://doi.org/10.1038/s41574-021-00517-x
Stener-Victorin E, Teede H, Norman RJ, et al., 2024. Polycystic ovary syndrome. Nat Rev Dis Primers, 10(1):27. https://doi.org/10.1038/s41572-024-00511-3
Stener-Victorin E, Deng Q, 2025. Epigenetic inheritance of pcos by developmental programming and germline transmission. Trends Endocrinol Metab, 36(5):472-481. https://doi.org/10.1016/j.tem.2024.12.002

Not for publication

Swindells EOK, Alesi LR, Stringer JM, et al., 2026. Guidelines for quantifying ovarian follicles: Every follicle counts. Reproduction, 171(3) https://doi.org/10.1093/reprod/xaag002

Szklarczyk D, Kirsch R, Koutrouli M, et al., 2023. The string database in 2023: Protein-protein association networks and functional enrichment analyses for any sequenced genome of interest. Nucleic Acids Res, 51(D1):D638-D646. https://doi.org/10.1093/nar/gkac1000

Tata B, Mimouni NEH, Barbotin AL, et al., 2018. Elevated prenatal anti-mullerian hormone reprograms the fetus and induces polycystic ovary syndrome in adulthood. Nat Med, 24(6):834-846. https://doi.org/10.1038/s41591-018-0035-5

Teede HJ, Tay CT, Laven J, et al., 2023. Recommendations from the 2023 international evidence-based guideline for the assessment and management of polycystic ovary syndrome†. Hum Reprod, 38(9):1655-1679. https://doi.org/10.1093/humrep/dead156

Teede HJ, Khomami MB, Morman R, et al., 2026. Polyendocrine metabolic ovarian syndrome, the new name for polycystic ovary syndrome: A multistep global consensus process. Lancet, 407(10545):2329-2339. https://doi.org/10.1016/S0140-6736(26)00717-8

Thompson MD, Kang J, Faerber A, et al., 2022. Maternal obesogenic diet regulates offspring bile acid homeostasis and hepatic lipid metabolism via the gut microbiome in mice. Am J Physiol Gastrointest Liver Physiol, 322(3):G295-G309. https://doi.org/10.1152/ajpgi.00247.2021

Torstensson S, Ascani A, Risal S, et al., 2024. Androgens modulate the immune profile in a mouse model of polycystic ovary syndrome. Adv Sci (Weinh), 11(28):e2401772. https://doi.org/10.1002/advs.202401772

Turner MD, Nedjai B, Hurst T, et al., 2014. Cytokines and chemokines: At the crossroads of cell signalling and inflammatory disease. Biochim Biophys Acta, 1843(11):2563-2582. https://doi.org/10.1016/j.bbamcr.2014.05.014

Wang C, Ding C, Hua Z, et al., 2020. Cangfudaotan decoction alleviates insulin resistance and improves follicular development in rats with polycystic ovary syndrome via igf-1-pi3k/akt-bax/bcl-2 pathway. Mediators Inflamm, 2020:8865647. https://doi.org/10.1155/2020/8865647

Wang F, Qualls AE, Marques-Fernandez L, et al., 2021. Biology and pathology of the uterine microenvironment and its natural killer cells. Cell Mol Immunol, 18(9):2101-2113. https://doi.org/10.1038/s41423-021-00739-z

Wang J, Zhao X, Wan YY, 2023. Intricacies of tgf-beta signaling in treg and th17 cell biology. Cell Mol Immunol, 20(9):1002-1022. https://doi.org/10.1038/s41423-023-01036-7

Wu L, Zhang H, Fan M, et al., 2022. Efficacy and safety of cangfu daotan decoction in patients with polycystic ovary syndrome: A systematic review and meta-analysis. Evid Based Complement Alternat Med, 2022:4395612. https://doi.org/10.1155/2022/4395612

Yang Y, Zhou J, 2025. Effects of citrus on oxidative stress and lipid metabolism modulation: Its potential for improving female reproductive health. J Zhejiang Univ Sci B, 26(8):763-777. https://doi.org/10.1631/jzus.B2500127

Yi W, Li X, Chen K, et al., 2021. Effects of cangfu daotan decoction on obese polycystic ovary syndrome and its mechanism. Steroids, 165:108740. https://doi.org/10.1016/j.steroids.2020.108740

Yin H, Duo H, Li S, et al., 2025. Unlocking biological insights from differentially expressed genes: Concepts, methods, and future perspectives. J Adv Res, 76:135-157. https://doi.org/10.1016/j.jare.2024.12.004

**Supplementary information**

Materials and methods; Tables S1-6; Figs. S1-3.

Under Review